

Article

Photomechanical Structures Based on Porous Alumina Templates Filled with 9-Methylanthracene Nanowires

Adam J. Berges ¹, Wangxiang Li ¹, Wenwen Xu ², Fei Tong ^{1,†}, Rabih O. Al-Kaysi ³, Ryan C. Hayward ²
and Christopher J. Bardeen ^{1,*}

- ¹ Department of Chemistry, University of California, Riverside, CA 92521, USA; adam.berges@email.ucr.edu (A.J.B.); wangxiang.li@email.ucr.edu (W.L.); feitong@ecust.edu.cn (F.T.)
- ² Department of Chemical and Biological Engineering, University of Colorado Boulder, 3415 Colorado Ave, Boulder, CO 80303, USA; wenwen.xu@colorado.edu (W.X.); ryan.hayward@colorado.edu (R.C.H.)
- ³ College of Science and Health Professions, King Saud bin Abdulaziz University for Health Sciences, and King Abdullah International Medical Research Center (Nanomedicine), Ministry of National Guard Health Affairs, Riyadh 11426, Saudi Arabia; kaysir@ksau-hs.edu.sa
- * Correspondence: christopher.bardeen@ucr.edu
- † Current address: School of Chemistry and Molecular Engineering, East China University of Science and Technology, Shanghai 200237, China.

Abstract: 9-Methylanthracene (9MA) undergoes a concerted [4 + 4] photodimerization in its crystal form that can be harnessed in order to generate photomechanical motions such as bending, twisting, and expansion. As described in this paper, 9MA nanowires were grown in anodic aluminum oxide (AAO) templates with the goal of using the crystal expansion to generate a net increase in the height of the composite disk. The growth conditions were optimized in order to raise the filling amount from 28% to 77% of the available volume in the porous AAO. A new experimental method for detecting motion, based on the analysis of data from a dynamically misaligned Michelson interferometer, was developed. Template bending was observed, showing that the photodimerization of the confined nanowires generated mechanical work, but no conclusive evidence for surface disruption or vertical translation was observed. Optical measurements, as well as atomic force and scanning electron microscopy, showed that incomplete filling, crystal orientation, and debris from template polishing likely prevented the observation of vertical actuation in these nanocrystal composites. This work highlights some of the practical challenges that are involved in creating photomechanical actuators using the organic–inorganic composite approach, with the two most significant being (1) the uniform filling of the porous template with the organic active material and (2) the removal of excess organic material from the template’s surface.



Citation: Berges, A.J.; Li, W.; Xu, W.; Tong, F.; Al-Kaysi, R.O.; Hayward, R.C.; Bardeen, C.J. Photomechanical Structures Based on Porous Alumina Templates Filled with 9-Methylanthracene Nanowires. *Crystals* **2022**, *12*, 808. <https://doi.org/10.3390/cryst12060808>

Academic Editor: Borislav Angelov

Received: 12 May 2022

Accepted: 2 June 2022

Published: 8 June 2022

Publisher’s Note: MDPI stays neutral with regard to jurisdictional claims in published maps and institutional affiliations.



Copyright: © 2022 by the authors. Licensee MDPI, Basel, Switzerland. This article is an open access article distributed under the terms and conditions of the Creative Commons Attribution (CC BY) license (<https://creativecommons.org/licenses/by/4.0/>).

Keywords: photomechanical crystals; nanowires; crystal growth; porous templates; photodimerization

1. Introduction

Photomechanical materials are designed to directly transform light into mechanical work [1,2]. Most organic photomechanical crystals and polymers rely on a photochemical mechanism, such as the cis-trans photoisomerization of azobenzene [3], in order to generate this work. In order to efficiently generate macroscopic amounts of work, the photoreactive molecules (photochromes) must be organized in some way [4]. This organization is accomplished in a polymeric matrix by incorporating the photochrome into a liquid crystal elastomer [5]. The use of a polymer matrix allows the facile creation of differently sized and shaped structures using well-established methods such as molding and photolithography. Alternatively, the photochromes can order by self-assembling into a neat molecular crystal [6–15]. The potential advantages of photomechanical crystals include their higher photochrome density and elastic modulus [16]. Unlike in the case of polymers, however, controlling the morphology of single crystals is very challenging

and typically a broad distribution of sizes and shapes is obtained. Furthermore, molecular crystals are prone to fracture due to the internal stress that is generated by the build-up of photoproduct regions, especially if the crystals are larger than a few microns [6,17,18]. They also tend to dissolve or degrade when exposed to organic solvents or air, respectively; although attempts to encase crystals in protective layers of graphene [19], polymers [20], or metal organic frameworks [21] have had some success. Given these challenges, it is not obvious how to incorporate single crystals into practical actuator devices, despite their potential advantages.

We recently developed a composite approach to photomechanical materials in which the organic crystal component is organized inside a porous inorganic host [22,23]. The host material was a commercially produced anodic aluminum oxide (AAO) disk with nominal 200 nm diameter channels that permitted the growth of oriented crystalline nanowires. By using diarylethene photochromes that undergo a ring-closing isomerization [24], the photoreaction of the organic component resulted in the composite structure undergoing a reversible bending motion. A milligram of this organic could reversibly lift 10 g or more. The bending templates are based on a bimorph structure of which the bottom part is converted into photoproduct while the top part remains unreacted (Figure 1a). The strain between the reactant and product domains leads to in-plane stress that is alleviated by bending. This mechanism of actuation was necessitated by the fact that only a thin layer near the surface could be isomerized by the input light. Diarylethene is a “positive” photochrome whose ring-closed isomer strongly absorbs the UV radiation, preventing it from penetrating throughout the template. If 100% conversion of the organic component could be achieved, it could enable different modes of actuation. For example, if the conversion of the organic component leads to crystal expansion, this could be utilized to make a composite in which the nanowires generate a concerted upward push (Figure 1b), rather than bending.

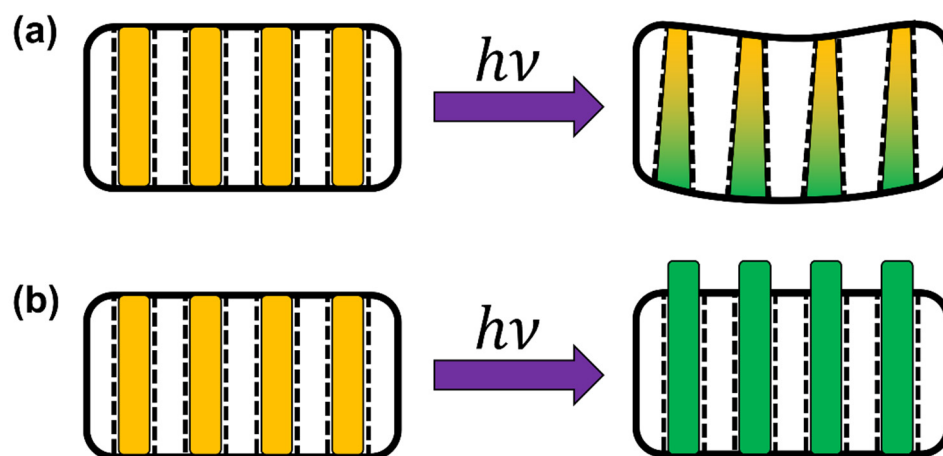


Figure 1. Schematic representation of the two possible methods of actuation in the organic-template system, (a) partial reaction of the crystal causing a change in curvature of the template and (b) full reaction of the crystal causing extension of organic nanorods through the surface of the template.

In order to create the composite photomechanical structure that is outlined in Figure 1b, several challenges must be overcome. First, the template must be completely filled with the organic, since any void spaces would serve to absorb the expansion inside of the channels, rather than forcing it outside of the template. Second, a “negative” photochromic reaction is required in order to allow the reaction to proceed to 100% completion [25], since a photoproduct that absorbs the excitation light will prevent it from reaching the unreacted portions of the sample, resulting in a bending bimorph as seen for the diarylethene reaction. Finally, the organic crystal must grow in an orientation that allows it to expand along the pore axis and not perpendicular to it.

In this paper, we describe our efforts to realize the actuator structure that is shown in Figure 1b by utilizing crystalline 9-methylanthracene (**9MA**), a prototypical photomechanical material whose crystal structure, growth habits, and reactivity have been extensively characterized by our group and others [26–31]. Our goal is to fill AAO templates (Anodisc) with **9MA** monomer and then convert it to its photodimer form. This conversion should result in an elongation along the monomer *c*-axis and the projection of this axis onto the nanowire axis should lead to a net increase in the height of the composite disk. It turns out that, in a real system, multiple nonidealities, including partial filling, crystal orientation, and debris from template polishing, all conspire to prevent the scenario that is illustrated in Figure 1b from being realized. While we observed template bending, showing that the photodimerization generates mechanical work, there was little sign of the surface disruption or vertical translation that would indicate that the wire elongation can be harnessed in order to create a linear translation. This work highlights some of the practical challenges that are involved in creating robust, reproducible actuators using the organic–inorganic composite approach, with the biggest one being how to uniformly fill the porous template with the organic active material. Future research directions which may be pursued in order to overcome these challenges are discussed.

2. Experimental

2.1. Sample Preparation

The crystal growth solutions were prepared by adding approximately 5 mg of solid **9MA** (98%, Sigma Aldrich, Burlington, MA, USA) to a glass vial containing 50 μL CHCl_3 . The solution was then sealed in the vial and sonicated for 5 min in a room temperature water bath. An empty AAO template (Whatman Anodisc inorganic filter membrane, 13 mm diameter with a 0.2 μm pore diameter purchased from Whatman, UK) was wetted with CHCl_3 before it was placed on the PTFE stage in the solvent annealing apparatus. While the template was still wet, the **9MA** solution was quickly added on top of the template and a measured volume of CHCl_3 was added to the Kimwipe which was present below the sample stage (see Supporting Information for more details on the apparatus). The solvent was allowed to evaporate at room temperature overnight, after which the template was hand-polished using a series of lapping papers (9 μm Al_2O_3 , 5 μm SiC, 2 μm Al_2O_3 , 1 μm Al_2O_3 , and 0.3 μm Al_2O_3). Each face of the template was polished until it appeared to be shiny and uniform.

In order to make the AAO surface hydrophobic, we used previously developed methods to functionalize the surface with carboxylic acids [32]. Lauric acid ($\geq 98\%$ Sigma Aldrich) was dissolved in denatured laboratory-grade ethanol at a concentration of 20 g/L. The solution was added to a 10 mL beaker and heated to 55 $^\circ\text{C}$. Empty AAO templates were placed upright in the beaker, supported by a hollow PTFE cylinder, and the solution was stirred for 30 min. Afterwards, the templates were rinsed separately in Millipore water and fresh ethanol before drying in an oven at 80 $^\circ\text{C}$ for 15 min. The same procedure was used for 3-phenylpropionic acid; however, this additional process started with a concentration of 15 g/L in ethanol.

2.2. Characterization

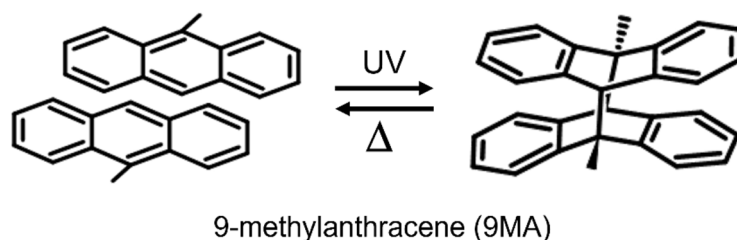
The water contact angles of the functionalized templates were measured using a Kruss D04010 EasyDrop system (Matthews, NC, USA) with a 50 μL droplet of water. Grazing incidence wide-angle X-ray diffraction (GIWAXS) experiments were performed using a Ganesha SAXS-LAB (Holyoke, MA, USA) instrument at room temperature. The X-rays ($\lambda = 1.54 \text{ \AA}$, Cu $\text{K}\alpha$ radiation) were incident at an angle of 2 $^\circ$ to the sample's surface in order to reveal the crystalline plane distribution with respect to the sample's normal direction. A slice of **9MA**-filled AAO template (3 mm \times 1 mm) was mounted on a Thorlabs Rotation Stage (MSRP01, purchased from ThorLabs, New Jersey, NJ, USA). A Pilatus 300K detector was used to collect the 2D diffraction pattern. The sample to detector distance was 86.55 mm. All the GIWAXS raw data were processed using SAXSGUI software.

The template surface was imaged using both scanning electron microscopy (SEM) and atomic force microscopy (AFM). For the SEM measurements, polished AAO templates were cut into quarters with a razor blade. Two portions of the template were exposed to UV (405 nm laser) while the remaining pieces were kept in the dark as reference samples. The samples were then fixed to a glass slide using polyimide tape before coating with Au using electron beam evaporation (Temescal BJD 1800, Santa Clara, CA, USA). The samples were imaged under a 10.0 kV electron beam in a Zeiss Leo XB 1540 microscope (White Plains, NY, USA). For the AFM measurements, filled templates were fixed to a magnetic stage with double-sided tape and imaged using a tapping mode AFM (AFM Probe NSG01, NT-MIDT Spectrum Instruments, Digital Instruments Nanoscope IIIA, South Jordan, UT, USA). The samples were irradiated in-situ using a 405 nm laser diode that was attenuated to 50 mW before passing through a diffuser. Higher laser intensities could not be used due to the damage that is caused by the heating of the gold-coated SiC probe tip.

In order to measure the photoinduced deformation of the filled AAO templates, a modified Michelson interferometer was used. In one arm, a template filled with **9MA** was placed on top of a 1-inch diameter optical flat. A 1-inch diameter mirror (mass = 1.28 g) was then placed on top of the supported template. In the other arm, the reference beam was reflected off of a mirror that was positioned with a piezoelectric linear actuator (ThorLabs PE6, New Jersey, NJ, USA) that was driven by an MDT 694B controller (ThorLabs, New Jersey, NJ, USA). In order to measure the photoinduced motion of the mirror on top of the template, the AAO was irradiated from beneath using a 405 nm laser diode with an intensity of $20 \mu\text{W}/\text{mm}^2$. A 632 nm HeNe probe laser (Spectra Physics 155, Milpitas, CA, USA) was passed through a beam-splitter to the sample and reference mirrors and the reflected beams were recombined. For the angular displacement measurements, the beams were directed 4.9 m away to a wall where the displacement was measured with a set of calipers. For the interferometry measurements, the overlapping sample and reference beams were directed into a photodiode (ThorLabs SM1PD1A, New Jersey, NJ, USA) that was equipped with a 630 nm longwave pass filter.

3. Results

The **9MA** photodimerization reaction that provided the basis of the observed photomechanical response is shown in Scheme 1. In order to grow crystalline **9MA** nanowires in the AAO templates, we used a modified version of the slow solvent annealing method that has been developed previously [33] (Supporting Information, Figure S1). Briefly, the template was saturated with a concentrated solution of **9MA** in CHCl_3 , then placed into a bell jar along with a variable amount of CHCl_3 solvent in a Kimwipe. The diffusion of the solvent vapor to the suspended template allowed the **9MA** molecules to self-assemble in the AAO channels. After the solvent had completely evaporated from the bell jar (~24 h), the template was removed and polished so as to remove the excess **9MA** that was on the surface. The resulting disk is the composite photomechanical material, but the inorganic AAO host can also be dissolved in a 20% aqueous H_3PO_4 acid solution in order to obtain isolated organic nanowires.



Scheme 1. The [4 + 4] cycloaddition reaction that generates the **9MA** photodimer after exposure to UV light. The reaction can be reversed by application of heat, but since **9MA** sublimes readily at elevated temperatures it can be considered irreversible under ambient conditions.

The first question that we tried to address was whether the **9MA** had completely filled the void space within the template. We determined the skeletal density of the Al_2O_3 in an empty template to be $3.0 \pm 0.3 \text{ g/cm}^3$ (Supporting Information). By measuring the mass and volume, we calculated the void fraction to be 58% or $4.87 \times 10^{-3} \text{ cm}^3$ out of a total disk volume of $7.96 \times 10^{-3} \text{ cm}^3$, a result which is in good agreement with the previous estimates that have been reported in the literature [34]. Given the density of crystalline **9MA** of 1.01 g/cm^3 , this allowed us to estimate a maximum fill amount of 4.7 mg in a 12.7 mm diameter template. Using our standard solvent annealing Method 1 (in which 2000 μL of CHCl_3 was added to the Kimwipe), we only attained an average fill of 1.3 mg or 28%, as determined by the mass change of the filled template. Examination of the bell jar revealed that the excess solvent from the Kimwipe was condensing out of the vapor phase and redissolving the **9MA** that had been deposited in the template. In some cases, the recondensed solvent was flowing back down to the bottom of the bell jar and bringing the **9MA** with it. In order to minimize this effect, we reduced the amount of CHCl_3 that was added to the chamber from 2000 to 75 μL . This lower volume was the maximum amount that could completely fill the chamber volume of 180 cm^3 with vapor and avoid liquid condensation. Upon using this Method 2 with a lower volume of CHCl_3 , we no longer observed solvent condensation or **9MA** transport in the chamber. The average fill amount increased dramatically from 1.3 to 3.6 mg (77% of the maximum) after polishing.

In an attempt to further improve the filling of the AAO template, we functionalized the Al_2O_3 surface. Using a lauric acid treatment, we were able to make the surface more hydrophobic, increasing the H_2O surface contact angle from 0° to $>130^\circ$ (Supporting Information, Figure S3). This treatment visibly improved the wetting of the template during the initial deposition of the **9MA/CHCl}_3 solution, but surprisingly it did not change the amount of filling to an extent that was outside the experimental error. This lack of effect for the surface treatment was observed for both the high and low solvent exposure solvent annealing methods, as is summarized in Figure 2. The use of other carboxylic acid terminated molecules, like 3-phenylpropanoic acid, also had no discernible effect on the filling (Supporting Information, Figure S4).**

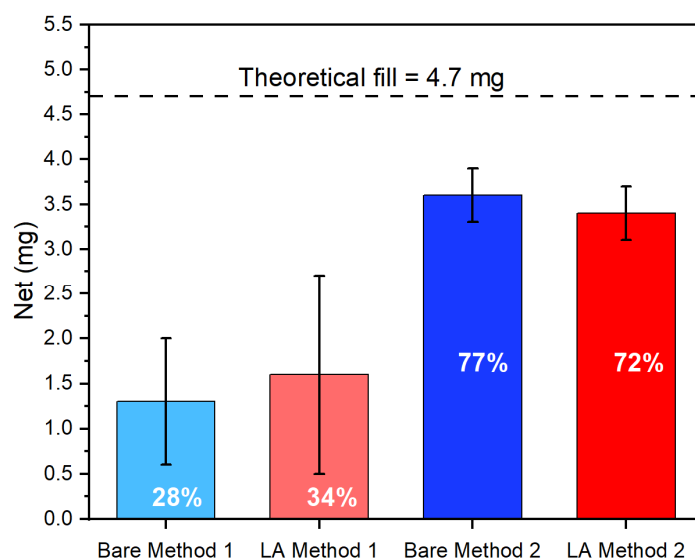


Figure 2. Measurements of the net mass of **9MA** embedded in the AAO template after annealing and polishing. From left to right: light blue from using Method 1 (excess solvent) in a bare template, light red from using Method 1 with a lauric acid (LA) covered template, dark blue from using Method 2 (no excess solvent) in a bare template, and dark red from using Method 2 in an LA covered template. Surface functionalization of the AAO template had a negligible impact compared to the solvent annealing process.

After solvent annealing and polishing, GIWAXS experiments on the filled templates were used in order to confirm that the **9MA** was crystalline. The measured GIWAXS pattern

for a filled template, along with the assignment of the diffraction peaks, is shown in Figure 3. The GIWAXS experiment acquired diffraction information across a range of angles, so it was sensitive to crystal planes with different orientations with respect to the surface plane. Based on the measured pattern, **b** is closely aligned with the surface normal and **a** is about 13 degrees off of the film plane's direction (indicated by a white line). Therefore, **c** in this case can be deduced to be almost parallel to the template's surface. Since the reciprocal axis **c** and real crystal axis *c* are only 6 degrees away from each other, we conclude that the *c*-axis is also almost parallel to the template surface. The average FWHM of the scattering peaks along the azimuthal direction in the samples is 3.7° , suggesting a high degree of alignment in relation to the film's normal direction.

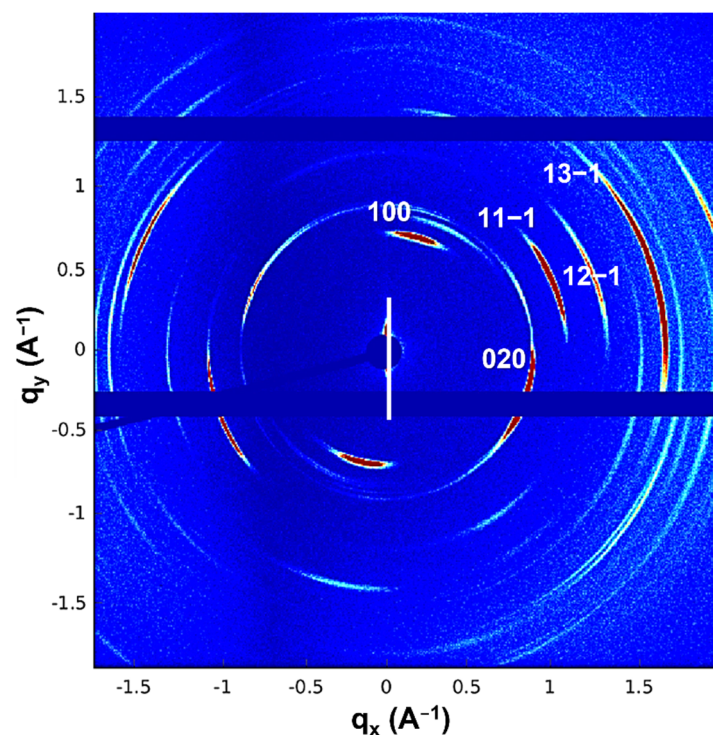


Figure 3. The GIWAXS pattern and accompanying face indexation for a $3\text{ mm} \times 1\text{ mm}$ sample cut from a **9MA**-filled template. The film plane direction is indicated by the white line near the origin. The FWHM of the scattering is 3.7° in the azimuthal direction, indicating that the sample is highly oriented along the film normal and thus inside the pore axis.

Since the expansion of **9MA** occurs along the *c*-axis [26,31] and this axis is apparently oriented perpendicularly to the long axis of the nanowires (i.e., parallel to the template's surface), we were concerned about whether the nanowires would elongate after light exposure, as shown in Figure 1b. Examination of the isolated nanowires confirmed their photomechanical elongation. An example of an individual nanowire response is shown in Figure 4. The nanowire exhibited an expansion of $\sim 7\%$ along its long axis, similar to the 7% expansion seen for the microcrystal plates along the crystal *c*-axis [31]. The expansion data and the GIWAXS data appeared to be contradictory, since the former is consistent with the nanowires growing along the *c*-axis, while the latter suggest that they grow perpendicular to the *c*-axis. However, this apparent contradiction assumes that polishing removes all of the excess surface crystallites and exposes only the vertically oriented nanorods that are embedded inside the AAO to the probing X-rays. As will be explained below, we found that the surface polishing procedure leaves a layer of mixed **9MA** crystals and AAO debris on the surface, which probably makes a strong contribution to the observed GIWAXS pattern.

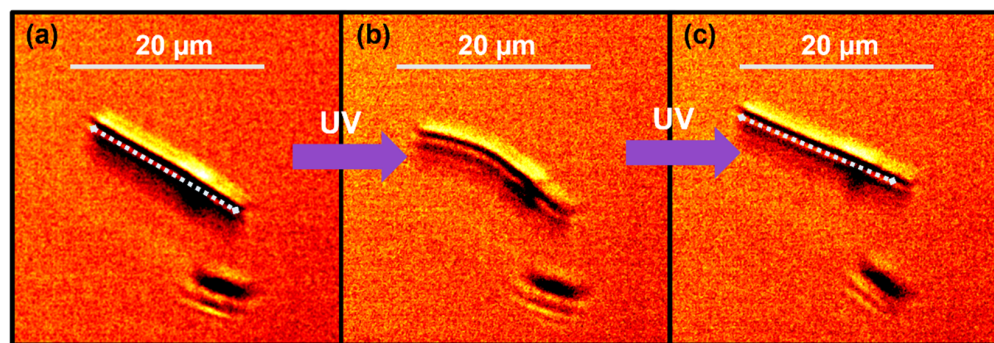


Figure 4. Optical microscope images of a **9MA** nanorod suspended in aqueous solution (a) before, (b) during, and (c) after exposure to UV light. The nanorod extends roughly 7% along its long axis.

We next determined whether the negative photochromic reaction of the **9MA** could enable 100% conversion inside the template. We assessed the conversion by exposing the template to varying durations of UV irradiation, followed by dissolving the organic component in a fixed volume of CHCl_3 . The amount of the remaining **9MA** could be determined using the Beer–Lambert law. We found that >98% of the initial **9MA** monomer had disappeared after 24 h of 405 nm exposure, with most of the reaction having been completed within the first 5 h (Supporting Information, Figure S5). This confirmed that the negative photochromic reaction of **9MA** could enable close to 100% conversion, even in the highly scattering AAO matrix.

Having found a method to significantly improve the templates' fill fraction, although not up to 100%, we proceeded to measure their photomechanical responses. In order to be sensitive to micron-scale motions, we placed the template under one mirror in a Michelson interferometer. The irradiation of the supported template from the bottom resulted in the movement of a mirror on top of the template, as illustrated in Figure 5a. Pure translational motion would result in an oscillatory intensity pattern at the output due to constructive and destructive interference, while the angular tilting of the mirror can be measured by its spatial displacement from the reference beam. If the situation that is illustrated in Figure 1b holds, we would expect to see pure translational motion as the nanowires extend above the template's surface. Figure 5b shows an example of the measured interferogram for a typical sample, along with images of the interferometer output before and after the irradiation. Both the interference and beam displacement are clearly present. The interferogram in Figure 5b can be modeled using the previously developed theory for interference signals in the presence of optical misalignment. In the experiments here, misalignment results from the photomechanical membrane moving one of the end mirrors. The equation for the integrated intensity at the interferometer output I_{photo} is given by [35,36]:

$$I_{\text{photo}} = A^2 \pi w^2 \left(1 + \exp \left(\frac{-(k^2 w^4 + 4(L(t) - z)^2) \alpha(t)^2}{8w^2} \right) \cdot \cos \left(kL(t) + \frac{k}{2}(L(t) - z) \alpha(t)^2 \right) \right) \quad (1)$$

where w is the beam waist, k is the wave number of the probe, z is the distance to the detector, L is the optical path difference, and α is the angular off-set. For the calculations that are used in this paper, $w = 1 \times 10^{-3}$ m, $k = \frac{2\pi}{632.8 \times 10^{-9}}$ m^{-1} , $z = 1$ m and we have neglected the factors due to the beam divergence and the Guoy phase shift. Neglecting these factors is justified when the beam diameter is much greater than the optical wavelength and there is no focusing inside the interferometer. Assuming a linear time dependence of the $\Delta\alpha$ and ΔL such that $L(t) = \Delta L(t - t_0)$ and $\alpha(t) = \Delta\alpha(t - t_0)$ where t_0 is the starting time for irradiation of the template, Equation (1) becomes:

$$I(t) = A^2 \pi w^2 \left(1 + \exp \left(\frac{-(k^2 w^4 + 4(\Delta L(t - t_0) - z)^2) (\Delta\alpha(t - t_0))^2}{8w^2} \right) \cdot \cos \left(k\Delta L(t - t_0) + \frac{k}{2}(\Delta L(t - t_0) - z) (\Delta\alpha(t - t_0))^2 \right) \right) \quad (2)$$

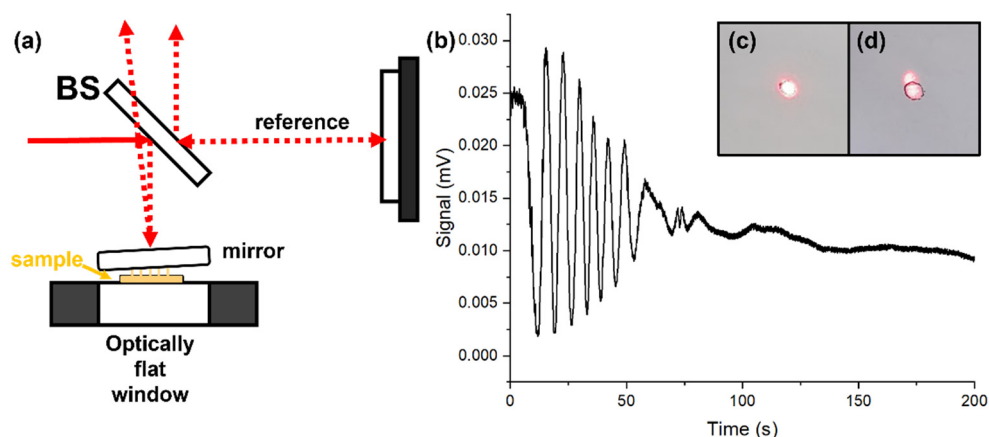


Figure 5. (a) Schematic of the interferometer set-up used to measure the photoinduced motion of the template. (b) Time-dependent photodiode signal from probe beams reflecting both interference and misalignment of probe beam due to angular tilt of the mirror during 405 nm irradiation. Complete misalignment causes a loss of signal that trends towards $\approx 50\%$ of the maximum intensity. The insets capture the (c) initial and (d) final positions of the probe beam 4.9 m away from the sample due to the misalignment.

Equation (2) assumes that ΔL and $\Delta\alpha$ are independent, but if a circular template of diameter D tilts by an angle $\Delta\alpha$, then it can be shown (see Supporting Information) that:

$$\Delta L(t) \approx \frac{D}{2} \times \Delta\alpha(t - t_0) \quad (3)$$

Using a value $\Delta\alpha = 4 \times 10^{-6}$ rad/s, Equation (2) can qualitatively reproduce the damped interferogram in Figure 5b, as shown in Figure 6. While there was considerable variability in the behavior of the filled templates (Supplementary Information, Figure S6), all of them showed some combination of $\Delta\alpha$ and ΔL evolution. In general, the $\Delta\alpha$ tilting was the dominant effect, with the output beams having been displaced by about 0.51 mrad on average.

The analysis of the beams' deflection indicates that most of the mirror displacement arose from tilting and not translation. Closer examination of the template surface before and after UV irradiation using SEM and AFM confirmed the absence of any significant wire expansion above the template's surface. Figure 7a,b show AFM images of a template surface before and after UV irradiation. A few small changes are seen in the surface's morphology after UV exposure, but the overall features are remarkably similar. The lack of dramatic changes can be contrasted with the dramatic reconstruction that can be observed after **9MA** single crystals undergo photoreaction [37]. For our samples, the surface features were not due to the presence of pure **9MA** but instead appeared to be a rough crust of debris that was left over from the polishing process. This debris can be seen more clearly in SEM images of the templates before and after filling and polishing. The array of pores in the pristine template in Figure 8a is completely submerged under a layer that is composed of both AAO fragments and the organic in Figure 8b. Careful examination of this crust shows that it contains broken nanowires and AAO fragments that have been aligned to the horizontal plane by the polishing process (Figure 8c). Even though we used Al_2O_3 abrasives for most of the polishing process, the underlying AAO has clearly sustained notable damage.

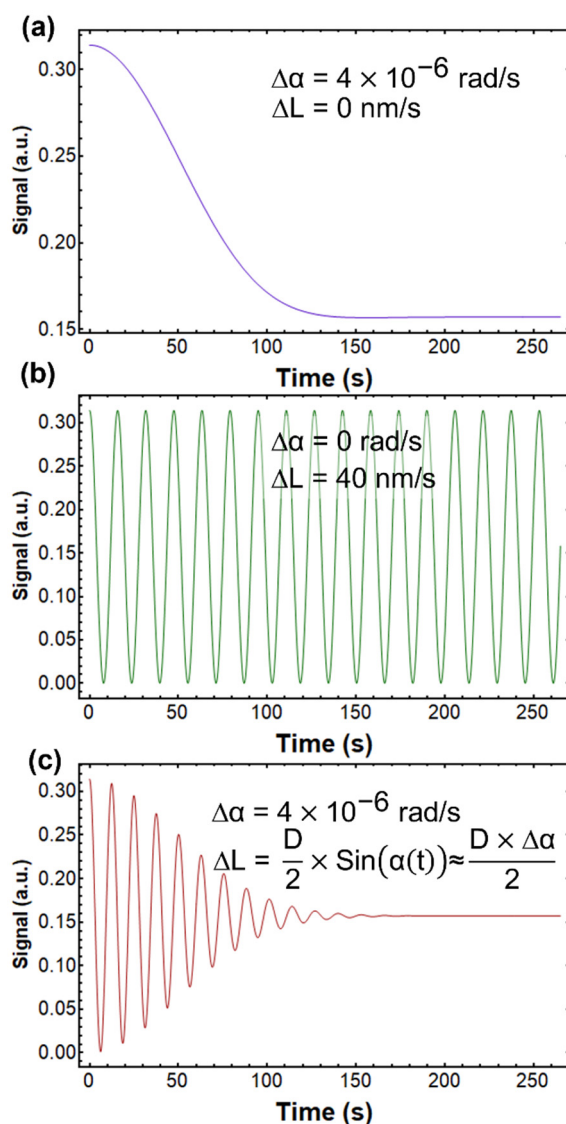


Figure 6. Simulated interferograms generated using Equation (2) with the parameters listed in the figures. Patterns caused by changes in either (a) the angular error or (b) the optical path difference do not agree with the data in Figure 5. Only when (c) both parameters change is an interferogram that is comparable to that in Figure 5 obtained. ΔL and $\Delta\alpha$ are as described in the main text and D is the diameter of the AAO template.

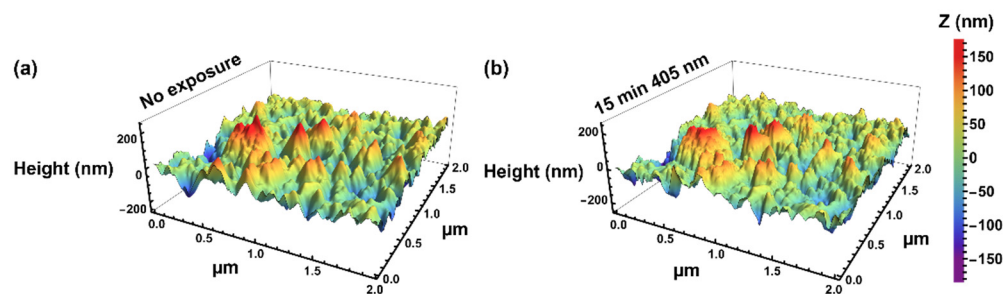


Figure 7. Atomic force microscope scan of a 9MA-filled template irradiated in-situ with a diffuse 405 nm laser. (a) before the 9MA was photo-dimerized and (b) after 15 min of exposure to 405 nm. There are slight changes in individual features but no obvious protrusions of nanowires from the surface.

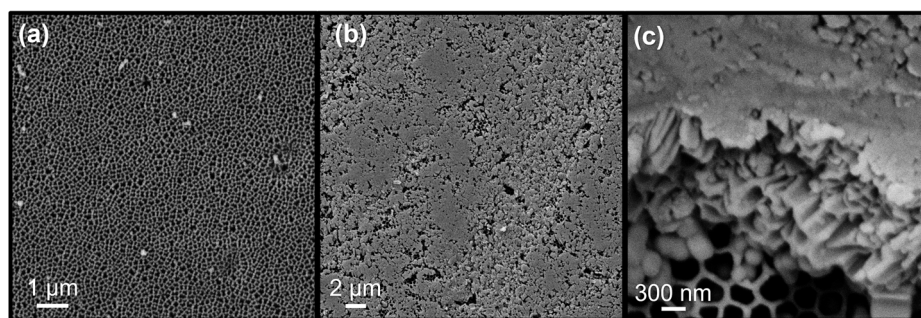


Figure 8. (a) SEM image of the pristine AAO surface in the absence of **9MA** and polishing. (b) At low magnification, SEM image of the polished surface of a **9MA**-filled template. (c) High magnification SEM image of the polished surface of a **9MA**-filled template, showing surface debris that covers the channels and has been smoothed by polishing.

The combination of the void spaces inside the template that were due to incomplete filling and a surface debris layer may explain why we did not see nanowires expanding out of the template in order to act as linear actuators. Given the choice of protruding up from the template by breaking through the surface debris layer or extending down into empty spaces in the interior of the template, the expanding nanowires probably chose the path of least resistance. The presence of broken nanowires lying parallel to the surface also explains why the GIWAXS measurements indicated that the crystal *c*-axis lay parallel to the template's surface. If the nanowires grow parallel to the *c*-axis, this axis should be normal to the template's surface for the vertical nanowires that are contained in the template. But if they are broken off and lie horizontal to the template surface, the *c*-axis would be in the direction that is indicated by the GIWAXS data. The presence of surface debris means that the GIWAXS experiment does not necessarily provide unambiguous information about the crystalline **9MA** that is inside the template's pores, but it does confirm that the surface layer that was left by polishing is both crystalline and highly oriented. The surface debris that is left after polishing has complicated the analysis of powder X-ray diffraction experiments on other organic crystals in AAO templates as well [38,39].

Although the negative photochromic reaction of crystalline **9MA** can be used to generate the deformation of a composite membrane, we did not observe the purely vertical displacement that we had hoped for. However, sufficient lateral forces were generated to deform and bend the template. The origin of this horizontal stress component is not obvious, but several possible factors may have contributed. First, the horizontal surface layer was strongly attached to the template due to the force of polishing. Expansion along the *c*-axis of the horizontally oriented nanorods on the bottom of the template could drive some bending motion via the usual bimorph mechanism. Second, there may be a population of crystallites inside the template the *c*-axis of which is not perfectly aligned along the pore, which would allow the expansion to have some projection along the horizontal axis. Finally, the smaller changes in the dimensions of the *a* and *b* crystal axes [31] may provide enough horizontal stress to slightly deform the template, irrespective of the *c*-axis expansion.

Our results highlight several challenges in the use of inorganic porous templates. First, it is difficult to achieve consistent, 100% filling using the solvent annealing method. Low filling fractions have also been found for the DAE photochrome in porous glass membranes, suggesting that this is a general problem. A completely different method of introducing the organic into the pores, perhaps melting the organic as opposed to using solvent annealing, might achieve higher filling but this may be more complicated to implement and may not lead to the same degree of crystallinity. Decreasing the thickness of the template and enlarging the pores may also facilitate organic filling. Although our simple surface functionalization did not improve the filling process, it is possible that a more sophisticated approach, perhaps using ligands that are tailored to the photochrome, could be more successful.

A second issue concerns the removal of the excess organic material that is left on the surface. For AAO, with a rough surface, we used high-grit polishing paper, but this method leaves a crust of dried slurry that can be several microns thick, as shown by the SEM images and the GIWAXS data. This crust can affect both the mechanical and light scattering properties. A gentler method that removes only the soft organic component would be desirable. Wiping the surface with a solvent soaked Kimwipe or cotton swab tended to remove the organic material from the surface and from inside the pores, so the right balance of mechanical and solvent forces must be found.

4. Conclusions

The results that are reported in this paper demonstrate that the photodimerization of 9MA can be used to power photomechanical motion in organic–inorganic hybrid actuator structures. A new experimental method for detecting motion, based on the analysis of a dynamically misaligned Michelson interferometer, has also been introduced. The results of this paper highlight the difficulties that are faced in the implementation of the organic–inorganic composite approach to photomechanical actuation. The reproducibility, linearity of motion, and overall response of the template were limited by our ability to completely fill the pores and remove debris from the surface. Taken together, the observations that are provided in this paper help to define the main challenges for the development of composite photomechanical materials that rely on molecular crystals as their active elements. Encouraging crystal growth in the porous host is a chemical problem, while removing excess organic material from the composite exterior is a materials processing problem. Both issues must be addressed in order to advance these composite materials toward practical applications as light-powered actuators.

Supplementary Materials: The following supporting information can be downloaded at: <https://www.mdpi.com/article/10.3390/cryst12060808/s1>, Figure S1: Flowchart detailing the new template filling procedure for 9MA in chloroform. Templates are pre-washed in chloroform before solution is added to the surface. Once dry, each sample is polished with 9 μm Al_2O_3 , 5 μm SiC, 2 μm , 1 μm , 0.3 μm Al_2O_3 lapping paper. Inset: photograph of the apparatus used; Figure S2: Cartoon of the apparatus used to measure the skeletal density of the AAO templates. Individual templates are supported in a mesh weigh boat and first measured in air, then completely submerged in the auxiliary liquid; Figure S3: (a,b) Contact angle measurements of a 50 μL water droplet on a LA-functionalized AAO surface. Samples demonstrate superhydrophobic surfaces with contact angles $\geq 130^\circ$. The untreated AAO templates are sufficiently hydrophilic to form contact angles below the limit of detection of the instrumentation. Side by side qualitative comparisons are captured in (c) using 100 μL of water added to each surface via micropipette; Figure S4: Comparison of the effect of surface functionalization on the AAO templates using the excess solvent method. Compared to the bare template, functionalizing the surface with lauric acid (LA) or 3-phenyl propanoic acid (3PPA) had a negligible effect outside of the margin of error; Figure S5: The percentage of the template that has been reacted when exposed to different durations of the UV source. In the first series, the beam spot size was approx. 96 mm^2 with a power density of $\approx 18 \mu\text{W}/\text{mm}^2$. In the second series, the beam was expanded with a diffuser to completely cover the template at the sample stage with a power density of $\approx 19.5 \mu\text{W}/\text{mm}^2$; Figure S6: Cartoon of the Michelson interferometer at the sample beam path. When the template deforms and tilts the mirror, the angular displacement ($\Delta\alpha$) and optical beam path difference (ΔL) can be coupled geometrically. This causes the sample beam path to tilt in the yz -plane, giving rise to the $E_2(x',y',z')$ field; Figure S7: Example interferograms collected from three different templates filled with 9MA. The dominant behavior of each interferogram is the angular off-set building during the exposure duration, leading to the damping of the fringe heights. This angular error appears to vary significantly from sample to sample.

Author Contributions: Conceptualization, A.J.B.; Methodology, A.J.B., W.L. and F.T.; Software, A.J.B.; Validation, W.X. and R.C.H.; Formal analysis, A.J.B. and C.J.B.; Writing—original draft, A.J.B. and C.J.B.; Investigation, A.J.B., W.L. and W.X.; Resources, A.J.B. and C.J.B.; Writing—review & editing, A.J.B., C.J.B., R.O.A.-K., W.X. and R.C.H.; Visualization, A.J.B. and W.X.; Project Administration, C.J.B.; Funding Acquisition, C.J.B. and R.C.H. All authors have read and agreed to the published version of the manuscript.

Funding: This work was supported by the Office of Naval Research through the MURI on Photomechanical Material Systems (ONR N00014-18-1-2624).

Institutional Review Board Statement: Not applicable.

Informed Consent Statement: Not applicable.

Data Availability Statement: The data presented in this study are available on request from the corresponding authors.

Conflicts of Interest: The authors declare that they have no conflict of interest.

References

1. White, T.J. *Photomechanical Materials, Composites, and Systems*, 1st ed.; Wiley: Hoboken, NJ, USA, 2017.
2. Kuzyk, M.G.; Dawson, N.J. Photomechanical materials and applications: A tutorial. *Adv. Opt. Photonics* **2020**, *12*, 847–1011. [[CrossRef](#)]
3. Taniguchi, T.; Asahi, T.; Koshima, H. Photomechanical Azobenzene Crystals. *Crystals* **2019**, *9*, 437. [[CrossRef](#)]
4. Kim, T.; Zhu, L.; Al-Kaysi, R.O.; Bardeen, C.J. Organic photomechanical materials. *ChemPhysChem* **2014**, *15*, 400–414. [[CrossRef](#)] [[PubMed](#)]
5. Ikeda, T.; Mamiya, J.; Yu, Y. Photomechanics of liquid-crystalline elastomers and other polymers. *Angew. Chem. Int. Ed.* **2007**, *46*, 506–528. [[CrossRef](#)]
6. Al-Kaysi, R.O.; Muller, A.M.; Bardeen, C.J. Photochemically driven shape changes of crystalline organic nanorods. *J. Am. Chem. Soc.* **2006**, *128*, 15938–15939. [[CrossRef](#)]
7. Kobatake, S.; Takami, S.; Muto, H.; Ishikawa, T.; Irie, M. Rapid and reversible shape changes of molecular crystals on photoirradiation. *Nature* **2007**, *446*, 778–781. [[CrossRef](#)]
8. Koshima, H.; Ojima, N.; Uchimoto, H. Mechanical motion of azobenzene crystals upon photoirradiation. *J. Am. Chem. Soc.* **2009**, *131*, 6890–6891. [[CrossRef](#)]
9. Morimoto, M.; Irie, M. A diarylethene cocrystal that converts light into mechanical work. *J. Am. Chem. Soc.* **2010**, *132*, 14172–14178. [[CrossRef](#)]
10. Naumov, P.; Kowalik, J.; Solntsev, K.M.; Baldridge, A.; Moon, J.-S.; Kranz, C.; Tolbert, L.M. Topochemistry and Photomechanical Effects in Crystals of Green Fluorescent Protein-like Chromophores: Effects of Hydrogen Bonding and Crystal Packing. *J. Am. Chem. Soc.* **2010**, *132*, 5845–5857. [[CrossRef](#)]
11. Bushuyev, O.S.; Tomberg, A.; Friscic, T.; Barrett, C.J. Shaping Crystals with Light: Crystal-to-Crystal Isomerization and Photomechanical Effect in Fluorinated Azobenzenes. *J. Am. Chem. Soc.* **2013**, *135*, 12556–12559. [[CrossRef](#)]
12. Nath, N.K.; Pejov, L.; Nichols, S.M.; Hu, C.; Saleh, N.; Kahr, B.; Naumov, P. Model for Photoinduced Bending of Slender Molecular Crystals. *J. Am. Chem. Soc.* **2014**, *136*, 2757–2766. [[CrossRef](#)] [[PubMed](#)]
13. Naumov, P.; Chizhik, S.; Panda, M.K.; Nath, N.K.; Boldyreva, E. Mechanically Responsive Molecular Crystals. *Chem. Rev.* **2015**, *115*, 12440–12490. [[CrossRef](#)] [[PubMed](#)]
14. Wang, H.; Chen, P.; Wu, Z.; Zhao, J.; Sun, J.; Lu, R. Bending, Curling, Rolling, and Salient Behavior of Molecular Crystals Driven by [2+2] Cycloaddition of a Styrylbenzoxazole Derivative. *Angew. Chem. Int. Ed.* **2017**, *56*, 9463–9467. [[CrossRef](#)]
15. Kitagawa, D.; Tsujioka, H.; Tong, F.; Dong, X.; Bardeen, C.J.; Kobatake, S. Control of Photomechanical Crystal Twisting by Illumination Direction. *J. Am. Chem. Soc.* **2018**, *140*, 4208–4212. [[CrossRef](#)]
16. Spackman, P.R.; Grosjean, A.; Thomas, S.P.; Karothu, D.P.; Naumov, P.; Spackman, M.A. Quantifying Mechanical Properties of Molecular Crystals: A Critical Overview of Experimental Elastic Tensors. *Angew. Chem. Int. Ed.* **2021**, *61*, e202110716. [[CrossRef](#)]
17. Takahashi, S.; Miura, H.; Kasai, H.; Okada, S.; Oikawa, H.; Nakanishi, H. Single-crystal-to-single-crystal transformation of diolefin derivatives in nanocrystals. *J. Am. Chem. Soc.* **2002**, *124*, 10944–10945. [[CrossRef](#)]
18. Bucar, D.K.; MacGillivray, L.R. Preparation and reactivity of nanocrystalline cocrystals formed via sonocrystallization. *J. Am. Chem. Soc.* **2007**, *129*, 32–33. [[CrossRef](#)]
19. Li, W.; Tierce, N.T.; Bekyarova, E.; Bardeen, C.J. Protection of Molecular Microcrystals by Encapsulation under Single-Layer Graphene. *ACS Omega* **2018**, *3*, 8129–8134. [[CrossRef](#)]
20. Xu, P.; Yu, Q.; Chen, Y.; Cheng, P.; Zhang, Z. Protective Coating with Crystalline Shells to Fabricate Dual-Stimuli Responsive Actuators. *CSC Chem.* **2022**, *4*, 205–213. [[CrossRef](#)]
21. Chiba, H.; Morimoto, M.; Irie, M. Stepwise Assembly of Ultrathin Poly(vinyl alcohol) Films on Photoresponsive Diarylethene Crystals. *Chem. Lett.* **2021**, *50*, 84–86. [[CrossRef](#)]

22. Dong, X.; Tong, F.; Hanson, K.M.; Al-Kaysi, R.O.; Kitagawa, D.; Kobatake, S.; Bardeen, C.J. Hybrid Organic-Inorganic Photon Powered Actuators Based on Aligned Diarylene Nanocrystals. *Chem. Mater.* **2019**, *31*, 1016–1022. [[CrossRef](#)]
23. Dong, X.; Guo, T.; Kitagawa, D.; Kobatake, S.; Palffy-Muhoray, P.; Bardeen, C.J. Effects of Template and Molecular Nanostructure on the Performance of Organic-Inorganic Photomechanical Actuator Membranes. *Adv. Funct. Mater.* **2019**, *30*, 1902396. [[CrossRef](#)]
24. Irie, M.; Fukaminato, T.; Matsuda, K.; Kobatake, S. Photochromism of Diarylene Molecules and Crystals: Memories, Switches, and Actuators. *Chem. Rev.* **2014**, *114*, 12174–12277. [[CrossRef](#)] [[PubMed](#)]
25. Aiken, S.; Edgar, R.J.L.; Gabbutt, C.D.; Heron, B.M.; Hobson, P.A. Negatively Photochromic Organic Compounds: Exploring the Dark Side. *Dye. Pigm.* **2018**, *149*, 92–121. [[CrossRef](#)]
26. Turowska-Tyrk, I.; Trzop, E. Monitoring structural transformations in crystals. 6. The [4+4] photodimerization of 9-methylanthracene. *Acta Cryst. B* **2003**, *59*, 779–786. [[CrossRef](#)]
27. Takegoshi, K.; Nakamura, S.; Terao, T. Solid-state photodimerization of 9-methylanthracene as studied by solid-state ¹³C NMR. *Solid State Nucl. Magn. Reson.* **1998**, *11*, 189–196. [[CrossRef](#)]
28. Mabied, A.F.; Muller, M.; Dinnebier, R.E.; Nozawa, S.; Hoshino, M.; Tomita, A.; Sato, T.; Adachi, S. A time-resolved powder diffraction study of in-situ photodimerization kinetics of 9-methylanthracene using a CCD area detector and parametric Rietveld refinement. *Acta Cryst. B* **2012**, *68*, 424–430. [[CrossRef](#)]
29. Kim, T.; Zhu, L.; Mueller, L.J.; Bardeen, C.J. Mechanism of Photoinduced Bending and Twisting in Crystalline Microneedles and Microribbons Composed of 9-Methylanthracene. *J. Am. Chem. Soc.* **2014**, *136*, 6617–6625. [[CrossRef](#)]
30. Salzillo, T.; Venuti, E.; Valle, R.G.D.; Brillante, A. Solid-state photodimerization of 9-methyl-anthracene. *J. Raman Spectrosc.* **2017**, *48*, 271–277. [[CrossRef](#)]
31. Morimoto, K.; Kitagawa, D.; Tong, F.; Chalek, K.; Mueller, L.J.; Bardeen, C.J.; Kobatake, S. Correlating Reaction Dynamics and Size Change during the Photomechanical Transformation of 9-Methylanthracene Single Crystals. *Angew. Chem. Int. Ed.* **2022**, *61*, e202114089. [[CrossRef](#)]
32. Norek, M.; Krasiński, A. Controlling of water wettability by structural and chemical modification of porous anodic alumina (PAA): Towards super-hydrophobic surfaces. *Surf. Coating Technol.* **2015**, *276*, 464–470. [[CrossRef](#)]
33. Al-Kaysi, R.O.; Bardeen, C.J. General method for the synthesis of crystalline organic nanorods using porous alumina templates. *Chem. Commun.* **2006**, *11*, 1224–1226. [[CrossRef](#)] [[PubMed](#)]
34. Abad, B.; Maiz, J.; Martin-Gonzalez, M. Rules to Determine Thermal Conductivity and Density of Anodic Aluminum Oxide (AAO) Membranes. *J. Phys. Chem. C* **2016**, *120*, 5361–5370. [[CrossRef](#)]
35. D’Agostino, G.; Robertsson, L. Relative beam misalignment errors in high accuracy displacement interferometers: Calculation and detection. *Appl. Phys. B* **2011**, *103*, 357–361. [[CrossRef](#)]
36. Smith, R.; Fuss, F.K. Theoretical Analysis of Interferometer Wave Front Tilt and Fringe Radiant Flux on a Rectangular Photodetector. *Sensors* **2013**, *13*, 11861–11898. [[CrossRef](#)]
37. Kaupp, G. Photodimerization of anthracenes in the solid state: New results from atomic force microscopy. *Angew. Chem. Int. Ed.* **1992**, *31*, 595–598. [[CrossRef](#)]
38. Chalek, K.R.; Dong, X.; Tong, F.; Kudla, R.A.; Gill, A.D.; Xu, W.; Yang, C.; Hartman, J.D.; Magalhaes, A.; Al-Kaysi, R.O.; et al. Bridging photochemistry and photomechanics with NMR crystallography: The molecular basis for the macroscopic expansion of an anthracene ester nanorod. *Chem. Sci.* **2021**, *12*, 453–463. [[CrossRef](#)]
39. Yang, C.; Zhu, L.; Kudla, R.A.; Hartman, J.D.; Al-Kaysi, R.O.; Monaco, S.; Schatschneider, B.; Magalhaes, A.; Beran, G.J.O.; Bardeen, C.J.; et al. Crystal Structure of the Meta-Stable Intermediate in the Photomechanical Crystal-to-Crystal Reaction of 9-Tert-Butyl Anthracene Ester. *CrystEngComm* **2016**, *18*, 7319–7329. [[CrossRef](#)]